Nanoscale

ROYAL SOCIETY OF CHEMISTRY

MINIREVIEW



Cite this: *Nanoscale*, 2024, **16**, 10551

# Recent advances in bismuth oxychalcogenide nanosheets for sensing applications

Amit Kumar Shringi, Rajeev Kumar and Fei Yan *

Received 26th February 2024,
Accepted 28th April 2024

DOI: 10.1039/d4nr00821a

rsc.li/nanoscale

This review offers insights into the fundamental properties of bismuth oxychalcogenides $Bi_2O_2X$ (X = S, Se, Te) (BOXs), concentrating on recent advancements primarily from studies published over the past five years. It examines the physical characteristics of these materials, synthesis methods, and their potential as critical components for gas sensing, biosensing, and optical sensing applications. Moreover, it underscores the implications of these advancements for the development of military, environmental, and health monitoring devices.

## 1. Introduction

Silicon's exceptional electronic properties, stability, and earth's crust abundance have cemented its dominance in the semiconductor industry since the 1950s.[1] Driven by extensive research and the booming demand for electronics, silicon technology has undergone rapid evolution and matured significantly over the years.. Silicon-based technologies downscaled to 5 nm by 2020 and further downscaling efforts are in progress.[2] But silicon as a 3D semiconductor seems to be hitting the downscaling limit and fabrication challenges. The reduced carrier mobility and power dissipation are the major challenges associated with silicon technology at lower feature sizes. The use of lower-dimensional semiconductors can be a potential solution for future electronics. Low-dimensional materials offer high carrier mobility, minimal scattering and can be downscaled up to 1 nm.[3] These low-dimensional semiconductors show multifunctional properties and can be used for other semiconductor device applications such as photodetection, sensing, energy storage and memory.[4–7]

In 2004, the discovery of graphene and its surprisingly excellent properties gained huge attention from researchers and industry towards two-dimensional (2D) materials.[8] 2D materials have an atomic-level arrangement and strong interatomic bonds along the two dimensions. The motion of electrons and phonons is confined in the 2D plane with the atomically thin third dimension. The atomically thin 2D materials show fascinating optical, electronic and mechanical features in comparison with their 3D allotropes.[9,10] Layer-modulated band gap transition and improved atomic contribution for the exposed surface in 2D materials make them the material of choice for optoelectronic and sensing applications. As a contribution of years of research, a variety of 2D materials have been explored with diverse electronic properties ranging from conductors to insulators. The family of 2D materials evolved over the years, and along with graphene, it involves 2D transition metal dichalcogenides (TMDs), MXenes, graphitic carbon nitride (g-$C_3N_4$), black phosphorus (BP), hexagonal boron nitride (hBN), layered perovskites, and metal phosphorus trichalcogenides.[11–17] These 2D materials have been explored and studied to investigate their material properties and potential for sensing, optoelectronic, storage, catalysis, memory and dielectric applications. Besides the excellent properties

*Department of Chemistry and Biochemistry, North Carolina Central University, Durham-27707, North Carolina, USA. E-mail: fyan@nccu.edu*

**Fei Yan**

*Fei Yan is a full professor in the Department of Chemistry and Biochemistry at North Carolina Central University. He obtained his Ph.D. from the State University of New York at Binghamton, followed by postdoctoral stints at the University of Michigan and Oak Ridge National Laboratory. Subsequently, he held positions as an analytical chemist at ATMI, Inc., and as a senior research scientist at Duke University. Throughout his career, he has directed projects supported by the National Science Foundation, the Department of Defense, the Department of Education, RTI International, and the North Carolina Space Program. His research centers on the development of low-dimensional nanomaterials for applications in chemical and biological sensing, photodetection, environmental remediation, as well as energy storage and conversion.*

described above, studies also show the limitations associated with these 2D materials. 2D TMDs offer a layer-modulated bandgap but these materials suffer from low room temperature carrier mobility, thus limiting their use.[18–20] On the other hand, mobility for graphene (>10 000 $cm^2 V^{-1} s^{-1}$) is very high, but a small on/off ratio due to the zero bandgap is a limiting factor for electronic uses.[21,22] Despite its excellent mobility and wide band gap tunability, BP's practical application as a semiconductor is hindered by limitations in stability and processability.[23,24] Most of these 2D materials are van der Waals (vdW) materials and their interlayer gap leads to high air sensitivity, instability and poor performance. The limitations associated with 2D materials limit their use in sensing applications. Hence, it is a requirement of time to explore, design and investigate new 2D materials with tunable electronic properties, high carrier mobility, processability and environmental stability for the realization of next-generation semiconductor devices.

Recently, novel 2D bismuth oxychalcogenides (BOXs) have caught significant attention due to their excellent physical and chemical properties such as high carrier mobility, environmental stability, band gap tunability and quick response to external signals.[25,26] BOXs comprise alternate stacks of $[Bi_2O_2]^{2+}$ and $[X]^{2-}$(X = S, Se, Te) that are adhered through weak electrostatic force. Due to the excellent absorption of light and bandgaps ranging from 0.11 to 1.6 eV, BOXs have been extensively explored for photodetection applications.[27] BOXs offer high mobility under ambient conditions with a decent band gap range, which makes them the material of choice for the fabrication of resistive sensors for room temperature detection having a high signal-to-noise ratio.[28,29] Furthermore, the recent progress in wafer-scale growth of crystalline $Bi_2O_2Se$ shows the potential of integration of these materials with Si technology in the near future.[30]

The ultrahigh carrier mobility, bandgap range, and excellent stability towards environmental conditions make BOXs a material of choice compared to other semiconductors for sensing and optoelectronic applications. In recent years many synthesis approaches such as sol–gel, hydrothermal, chemical vapor deposition (CVD), molecular beam epitaxy (MBE), *etc.* have been explored for the realization of BOXs for different applications. The theoretical and experimental observations from recent reports show the potential of these materials as sensors for gas, bio, electrochemical and optical sensing.

This review explores recent advancements in BOXs, focusing on synthesis, growth techniques, and their potential for sensing applications. The different synthesis approaches including CVD, pulsed laser deposition (PLD) and exfoliation will be discussed. The crystal structure, electronic band structure and other material and electronic properties like carrier mobility, optical properties and ferroelectricity are briefly discussed for a general understanding of material behaviour towards different applications. In the next section, we discuss the most recent reports on BOXs-based sensing applications. For clarity and ease of understanding, we have categorized sensing applications into three main areas: gas sensing, biosensing, and optical sensing.

# 2. Atomic structure and material properties

## 2.1 Atomic structure

BOXs are non-vdW layered materials where each unit consists of two $[Bi_2O_2]$ layers between three atomic layers of chalcogen elements. The monolayer thick BOXs have one $[Bi_2O_2]$ cation layer between two chalcogen anion layers where 50% of chalcogen atoms of the chalcogen layer are shared with another monolayer and have a covalent bond with weak electrostatic interaction between layers. The atomic representation of BOXs is given in Fig. 1a. According to the atomic arrangement, $Bi_2O_2S$ crystals have an orthorhombic structure and the *Pnnm* space group ($a$ = 3.874 Å, $b$ = 3.84 Å and $c$ = 11.92 Å) whereas $Bi_2O_2Se$ and $Bi_2O_2Te$ have a tetragonal crystal structure with the *I*3/*mmm* space group. The lattice parameters are $a = b$ = 3.88 Å, $c$ = 12.16 Å and $Z$ = 2 for $Bi_2O_2Se$ and $a = b$ = 3.98 Å, $c$ = 12.70 Å for $Bi_2O_2Te$. Bulk BOXs crystals can be cleaved or exfoliated along the $c$-axis because of their non-neutral layered structure and appear as a broken zipper structure where half of the chalcogen atoms are shared by each part of the $BiO^+$ layer as shown in Fig. 1b.[31]

## 2.2 Electronic band structure and optical properties

Wu *et al.* reported the theoretical calculations to predict the electronic band structure of BOXs. The calculated values as shown in Fig. 1c–e are 1.25 eV for $Bi_2O_2S$, 0.89 eV for $Bi_2O_2Se$ and 0.16 eV for $Bi_2O_2Te$.[32] All three compounds show an indirect band gap. The experimental band gaps calculated using the Tauc plot show values of 1.3 eV to 1.5 eV referred to in different reports on $Bi_2O_2S$.[33,34] Considering the indirect nature of the band gap, the experimental band gaps reported are 1.38 eV to 1.67 eV for $Bi_2O_2Se$.[35,36] The optical band gap of $Bi_2O_2Te$ is still unknown due to the synthesis complexity in producing bulk and large-area samples.

## 2.3 Carrier concentration and mobility

A theoretical report shows that the ultrahigh electron mobility can be up to 26 699 $cm^2 V^{-1} s^{-1}$ at 330 K for the $Bi_2O_2S$ monolayer but still hasn't been explored experimentally.[39] $Bi_2O_2Se$ shows an ultrahigh electron mobility of 20 000 $cm^2 V^{-1} s^{-1}$ and a carrier concentration of $5 \times 10^{18}$ $cm^{-3}$ at 2 K. However, a room temperature mobility of 313 $cm^2 V^{-1} s^{-1}$ and a carrier density of $11 \times 10^{18}$ $cm^{-3}$ were reported.[40] Temperature- and thickness-dependent mobilities for $Bi_2O_2Te$ are presented in Fig. 1f. A carrier mobility of 303 $cm^2 V^{-1} s^{-1}$ and a carrier density of $1 \times 10^{13}$ $cm^{-3}$ at RT are reported for 8.9 nm thick $Bi_2O_2Te$ nanosheets.[38] The experimental results show variation in mobility and carrier density and it strongly depends on different parameters like thickness, defect density and temperature. It is still desirable to develop advanced growth and modification strategies to achieve ultrahigh mobility and high carrier density at RT.

The high mobility in BOXs compared to that in other semiconductors led to the donor states lying above the lowest con-

 

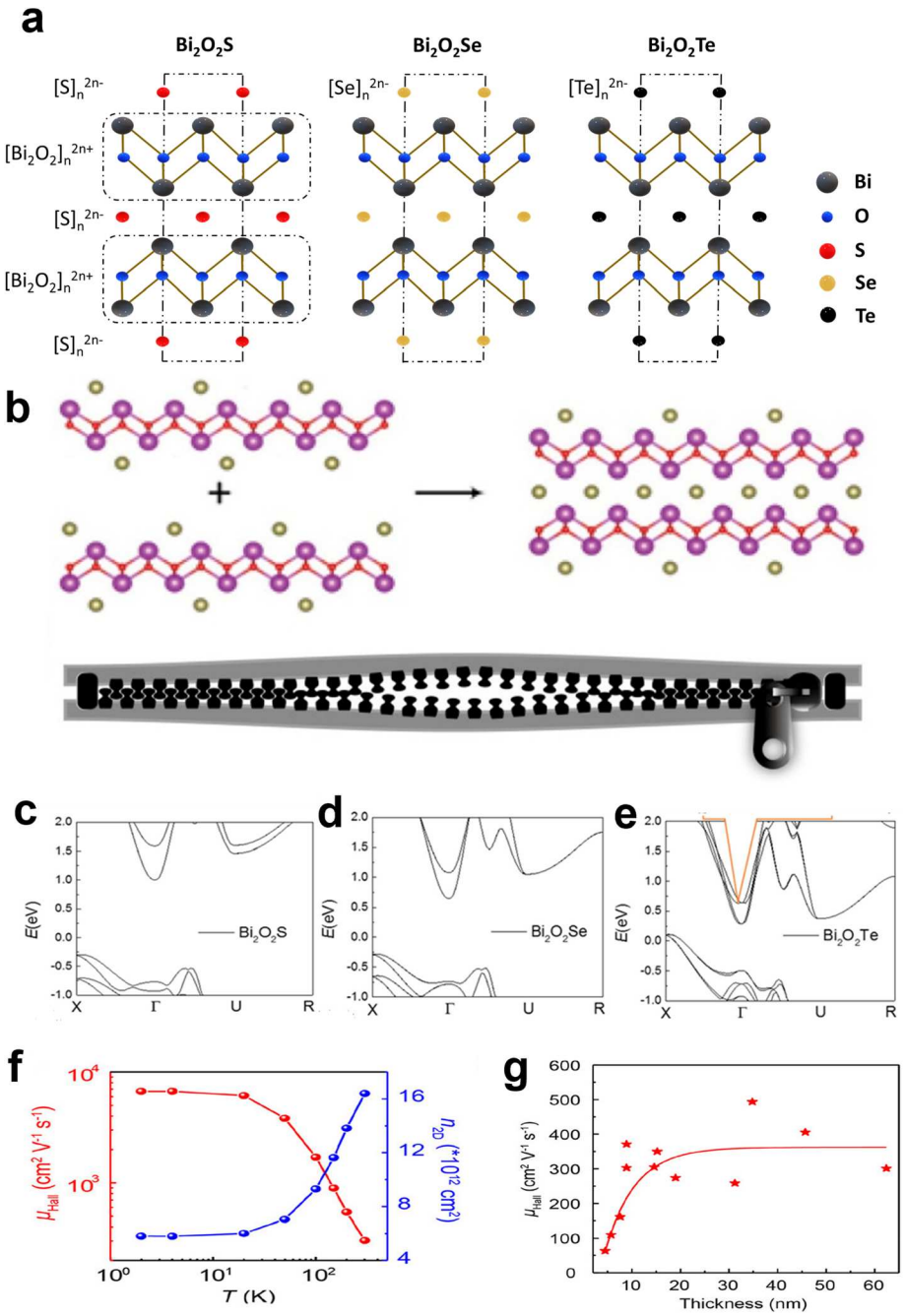


**Fig. 1** (a) Crystal structures of $Bi_2O_2S$, $Bi_2O_2Se$ and $Bi_2O_2Te$. (b) Scheme of a bilayer $Bi_2O_2Se$ formed by two monolayers and a zipper model. Reproduced with permission.[31] Copyright 2019, American Chemical Society. Electronic band structures of (c) $Bi_2O_2S$, (d) $Bi_2O_2Se$ and (e) $Bi_2O_2Te$. Reproduced with permission.[32] Copyright 2019, American Chemical Society. (f and g) Temperature- and thickness-dependent carrier mobility of $Bi_2O_2Te$. Reproduced with permission.[38] Copyright 2022, American Chemical Society.

duction band. Fu *et al.* observed the spontaneous ionization of electrons from donor sites for $Bi_2O_2Se$ even without any thermal activation, resulting in reduced resistance upon reduction in temperature.[41] The spatial separation of the conduction channel from the ionized donor defects further suppresses the donor site led scattering, resulting in further increased electron mobility. They call this phenomenon spontaneous self-modulation doping. Building on this concept, Tong *et al.* demonstrated a 10-fold increase in transport lifetime within $Bi_2O_2Se$ due to suppressed electron backscattering, leading to ultrahigh electron mobility.[42]

### 2.4 Other properties

There are several other properties in addition to structural, electronic and charge mobility properties that have great significance in the application of a semiconductor material.

Ferroelectricity is an important property for a semiconductor material enabling its use in sensing, storage and energy applications. The existence of ferroelectricity has been predicted theoretically for BOXs.[32] It has been experimentally demonstrated for 2D $Bi_2O_2Se$ and $Bi_2O_2Te$ nanosheets, where they have spontaneous polarization and show switching under an external electric field.[43,44]

The environmental stability of a sensing material is an important factor to be taken care of and it has a direct relation to its real-time application. As discussed in the Introduction, 2D semiconductors like BP have excellent carrier mobility, but their environmental instability is a limiting factor for their use in environmental monitoring applications. On the other hand, 2D BOXs have been reported with ultrahigh carrier mobility and excellent stability under ambient conditions.[45,46] Stable electronic properties upon exposure to ambient conditions with high mobility make them promising materials for environmental monitoring applications.

The biocompatibility of nanomaterials is an important aspect to be considered before using them for health monitoring, water treatment and therapy applications. $Bi_2O_2Se$ nanosheets have been reported as a biosafe material for water treatment[47] and cancer therapy[48] and hence they can be used for biomedical and biosensing applications.

As these materials are new, a lot of effort is required to validate and establish the reason behind these properties. Due to limited experimental evidence, BOXs have not been studied for energy harvesting applications. BOXs exhibit excellent atmospheric stability compared to other 2D materials, while also maintaining excellent flexibility without compromising their electronic properties.

# 3. Synthesis of 2D BOXs

The performance of 2D material-based electronic devices highly depends on the quality of the synthesized material as it alters the chemical and physical properties of these materials. Hence, a lot of research efforts have been made over time to develop protocols for large-scale and low-cost synthesis or growth of high-quality 2D materials. To date, various approaches have been reported for the synthesis and growth of 2D BOXs. The synthesis approaches for 2D BOXs are broadly classified into two categories: bottom-up and top-down approaches. In bottom-up approaches of synthesis, the synthesis requires the chemical precursors of the constituent elements and other reducing and capping agents. Using this approach, the synthesis of a powdered material and direct film growth can be achieved. The bottom-up approach involves hydrothermal, solution-assisted, CVD, PLD, and molecular beam epitaxy (MBE) methods. The use of different synthesis approaches depends on the application and it significantly alters the cost of the process. Second, the top-down approach involves the exfoliation of nanosheets from the bulk material or a single crystal of the material. Mechanical exfoliation, liquid exfoliation and ion intercalation are typical examples of top-down methods. The force induced during different methods helps to overcome the weak interlayer bonds to get mono or few-layer nanosheets from the bulk material. In the coming subsections, we will discuss the various synthesis methods for the synthesis or growth of different BOXs species.

## 3.1 Bottom-up processes

**3.1.1 Hydrothermal method.** The hydrothermal reaction is a widely used synthesis method to obtain nanostructured materials. It offers a simple, low-cost, high yield and reproducible synthesis method. It uses a special closed reaction vessel to execute the synthesis reaction, where the reactions take place at elevated temperatures (80–240 °C) and very high pressure. High temperatures and pressures within the vessel facilitate the formation and recrystallization of the desired compound. The hydrothermal method offers both powder synthesis and direct growth on a substrate. Zhang *et al.* reported the composite molten salt approach for the synthesis of $Bi_2O_2Se$ nanosheets and analyzed the thermoelectric properties. They used $KNO_3$ and $LiNO_3$ (57.6 : 42.4) as composite molten salts.[49] Initially, 9 g of the salt composite, 1 mmol of $Bi(NO_3)_3{\cdot}5H_2O$ and 0.5 mmol of Se powder were placed and shaken in a 25 ml Teflon vessel for complete mixing of reactants. Furthermore, 2 mL of $N_2H_4{\cdot}H_2O$ and 5 mL of DI water were added and the sealed Teflon vessel with a stainless autoclave was put in a preheated oven at 200 °C for 24 h. After 24 h, the autoclave was naturally cooled and the obtained solid product was washed with DI water and ethanol using centrifugation. The obtained powder shows a sheet-like morphology with an approximate thickness of 120 nm. In 2020, Li *et al.* reported a mild hydrothermal route as shown in Fig. 2(a) for synthesizing $Bi_2O_2S$ and $Bi_2O_2Se$ nanosheets.[37] They used ammonium bismuth citrate, thiourea and sodium selenite as starting precursors for the reaction and KOH as a mineralizer. Bi and Se/S sources were dissolved in DI water in a stoichiometric ratio and KOH was added for obtaining an alkali environment. The solution was transferred and sealed in a hydrothermal reactor and the obtained powder was washed several times with DI water and ethanol. The obtained nanosheets have lateral sizes of over 2 μm and a thickness of ~5 nm (Fig. 2(b–e)).

In addition to the powder synthesis, direct growth of $Bi_2O_2S$ nanoflowers and sheets on FTO was reported by Rong *et al.* in the year 2022.[50] Equimolar (1 mmol) amounts of thiourea and $Bi(NO_3)_3{\cdot}5H_2O$ were dissolved in a mixture of ethylene glycol and DI water (1 : 1) for 5 minutes followed by the addition of 5 mmol of KOH with continuous stirring until a clear solution was obtained. The solution was transferred to a 50 mL Teflon vessel and a clean FTO substrate was placed at an angle of 30°. The sealed reactor was put in an oven for 3 h at 120 °C. Finally, the cooled substrate was taken out and washed with DI water and ethanol followed by natural drying. The gradual assembly of stacked nanosheets with an increased reaction time formed flower-like continuous morphologies. Recently, Zhang *et al.* reported the growth of $Bi_2O_2S$ nanosheets on FTO with a similar modified growth protocol.[51]

 

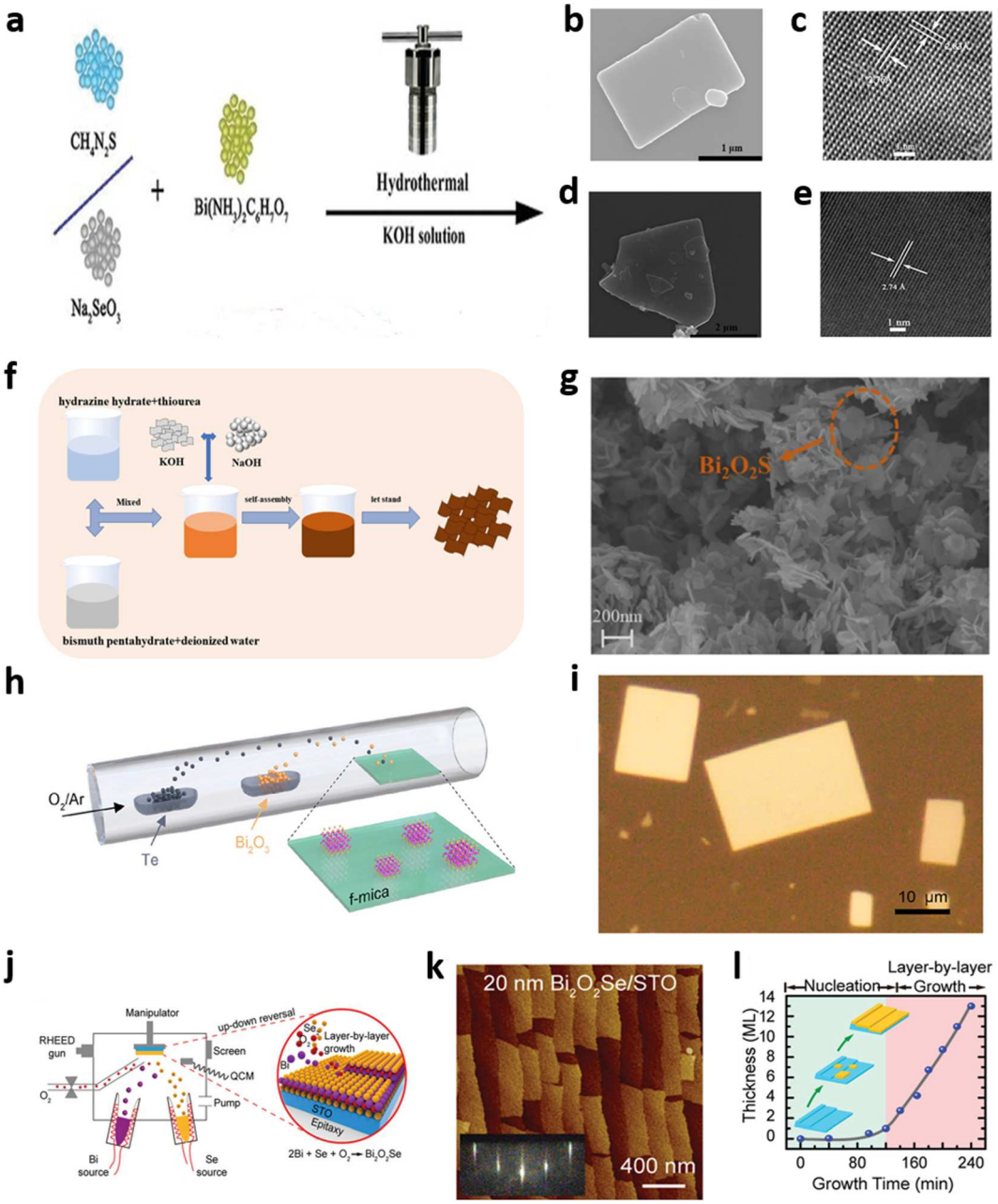


**Fig. 2** Synthesis and growth process of 2D BOXs: (a) schematic representation of the hydrothermal approach for 2D $Bi_2O_2S$ and $Bi_2O_2Se$ synthesis; (b and c) SEM and TEM for $Bi_2O_2S$; (d and e) SEM and TEM for $Bi_2O_2Se$ nanosheets. Reproduced with permission.[37] Copyright 2020, Wiley-VCH. (f and g) Solution-assisted synthesis of $Bi_2O_2S$ and SEM images of nanosheets. Reproduced with permission.[52] Copyright 2023, American Chemical Society. (h and i) Illustration of the CVD growth of 2D $Bi_2O_2Te$ and the optical image of $Bi_2O_2Te$ on mica. Reproduced with permission.[38] Copyright 2022, American Chemical Society. (j–l) Molecular beam epitaxy. Reproduced with permission.[29] Copyright 2020, Wiley-VCH.

**3.1.2 Solution-assisted synthesis.** The use of a reaction vessel and heating arrangement in the hydrothermal approach makes the process a little complex and costly. The solution-assisted synthesis method offers great simplicity and a low-cost and high-yield solution for the synthesis of various BOXs. The schematic representation of the process flow for the synthesis of $Bi_2O_2S$ nanosheets is shown in Fig. 2(f).[52] Among all the synthesis methods, the solution-assisted method gained more attention and was explored several times owing to the simple synthesis approach in a beaker over a hot plate (stirrer). Most of the solution-assisted synthesis reports addressed the room temperature synthesis protocol for BOXs, where they used $Bi(NO_3)_3{\cdot}5H_2O$ as a source of bismuth. On the other hand, different precursors have been reported as sources of chalcogens.

Chitara *et al.* reported the morphological dependence on the use of a reducing agent for the synthesis of $Bi_2O_2S$ nanostructures.[53] The use of hydrazine hydrate with thiourea led to

the formation of nanosheets, whereas in the absence of hydrazine hydrate, thicker nanoplatelets formed. They also observed a change in photoconductivity with the morphology change. Similarly, the use of Se powder with hydrazine hydrate instead of thiourea will lead to the formation of $Bi_2O_2Se$ nanosheets. Recently, Kumar *et al.* reported a microwave-assisted solution synthesis protocol for $Bi_2O_2Te$ nanosheets.[54] They observed the effect of microwave power on the crystallinity and other properties of the material.

**3.1.3 Chemical vapor deposition.** CVD is the most popular growth technique for the growth of various 2D materials and it gained significant attention for the growth of high-quality BOXs. It offers a controlled thickness and an atomically flat surface. A variety of precursors have been studied and optimized for the growth of BOXs. A carrier gas is used to transfer the vapor of the chemical precursor at an elevated temperature to grow the material on the desired solid substrate. A chemical reaction occurs in the gas phase before or during the growth on the substrate. Numerous efforts have been made to develop growth strategies for the growth of BOXs.

For the growth of BOXs, $Bi_2O_3$ and $Bi_2X_3$ (X = S, Se, Te) are the commonly used precursors. Furthermore, instead of bismuth chalcogenides, elemental precursors can also be used for the growth of BOXs. Ai *et al.* reported the low-pressure CVD growth of single crystalline 2D $Bi_2O_2Te$ nanoplates.[38] 0.5 g Te and 1 g $Bi_2O_3$ powder were evaporated in the presence of a carrier gas ($Ar/Ar:O_2$) to $Bi_2O_2$ and Te layers to form $Bi_2O_2Te$ as shown in Fig. 2(h and i). The ratio of the carrier gas (Ar to $O_2$) and the temperature show a significant effect on the phase evolution from $Bi_2Te_3$ to $Bi_2O_2Te$. Similarly for the CVD growth of $Bi_2O_2Se$, Chen *et al.* used $Bi_2O_3$ and $Bi_2Se_3$ powder and $N_2$ as a carrier gas.[55] The temperature of $Bi_2Se_3$ in the first zone was kept at 560 °C and that of $Bi_2O_3$ in the second zone was kept at 660 °C. The narrowing of the growth tube and the second zone temperature have a significant effect on the growth thickness. Khan *et al.* reported the vapor–solid deposition of $Bi_2O_2Se$ using CVD.[56] It uses bulk $Bi_2O_2Se$ powder prepared by a hydrothermal method. This approach reduces the requirement of multizone CVD and a controlled system. Single zone CVD is sufficient for the growth of 2D $Bi_2O_2Se$ using this approach.

**3.1.4 Pulsed laser deposition.** The PVD technique is used to deposit a thin film with the same stoichiometry as that of source (target). It uses a focused intense laser beam on the target to vaporize the material under a high vacuum atmosphere inside the chamber. The evaporated material inside the chamber gets deposited onto the substrate. It is a popular and very well-explored technique for the deposition of metal oxides and other materials. In recent years, a few reports published the deposition of $Bi_2O_2Se$ thin films by the PLD method.[57,58] Song *et al.* reported the deposition of a single crystalline $Bi_2O_2Se$ thin film on a single crystal $SrTiO_3$ substrate.[58] This technique offers a lower growth temperature for BOXs with good control of thickness and stoichiometry.

**3.1.5 Molecular beam epitaxy.** MBE is an advanced growth technique for epitaxial growth of semiconductor thin films with atomic thickness. It offers excellent control of thickness, crystal defects and stoichiometry. MBE growth has been studied and reported many times for the growth of bismuth chalcogenides and there is immense opportunity to explore the potential of MBE growth of BOXs. In 2019, Liang *et al.* reported an atomically thin $Bi_2O_2Se$ thin film using MBE (Fig. 2(j–l)).[29] The growth of the $Bi_2O_2Se$ thin film depends on growth parameters like temperature, Bi/Se flux ratio and oxygen ratio. The growth parameters were optimized to a $T_s$ of 290 °C and an oxygen pressure of $1 \times 10^{-4}$ mbar. The flux ratio needs to be maintained low to avoid the formation of any oxide phase during growth.

Growth temperature and oxygen pressure are crucial parameters for achieving controlled, phase-pure BOX layer thickness across the entire surface. For the uniform growth of BOXs, the growth temperature should lie between the evaporation temperatures of Bi and X atoms. The evaporation temperature of Te is higher than those of S and Se, and a higher growth temperature may be needed for the deposition of $Bi_2O_2Te$. The growth process for $Bi_2O_2Te$ and $Bi_2O_2S$ has not been explored so far but there are a lot of opportunities to grow these materials using the MBE technique.

**3.1.6 Other methods.** The growth of BOXs has been reported using several other methods including sputtering, MOCVD and LPCVD.[59,60] Sputtering involves the growth of bismuth chalcogenides followed by oxidation in air to form BOXs.

### 3.2 Top-down process

The ultrasonic exfoliation of crystals or the bulk material into 2D nanosheets or unit geometry using bath or tip sonication is an example of the top-down approach. Exfoliation can be used to reduce the particle size up to quantum dot (QD) dimensions.[61] Pan *et al.* reported a large area nanosheet exfoliation protocol of 20–30 layers thick using bulk $Bi_2O_2Se$.[62] Hui *et al.* reported exfoliated $Bi_2O_2Te$ nanosheets.[63] Tip sonication has been reported to achieve $Bi_2O_2Se$ QDs and has extensive use for surface functionalization for sensing applications.[64]

Ion intercalation is also a top-down process that involves the intercalation agent intercalating along the thickness of 2D materials and causing the expansion or weakening of the interlayer interaction. With shear force, the interlayer spacing increased further and led to the formation of thin layers from bulk samples. Lithium intercalation has been reported to exfoliate 2D $Bi_2O_2Se$ nanosheets using shear force in a liquid medium.[65] However, mechanical exfoliation (tape exfoliation) has not been reported so far for BOXs. The high inter-layer binding energy for BOXs compared to those of other vdW materials limits the use of scotch tape for exfoliation and advanced exfoliation methods are needed for mechanical exfoliation.

In contrast, a variety of synthesis and growth approaches have been explored for BOXs and each of the methods has its merits and demerits. As discussed in this section, the preparation method significantly alters the morphological and structural properties, such as crystallite size, nanostructure and

 

dimension. One can adopt suitable methods as per the requirement of the application. The top-down approaches, including liquid exfoliation, mechanical exfoliation and intercalation, are suitable for achieving BOX nanosheets with thickness ranging from a monolayer to hundreds of layers of the bulk material. Mechanical exfoliation offers ultrathin nanosheets of millimeter dimensions depending on an individual's expertise. Top-down approaches are low-cost methods and can process large amounts of samples with the same crystallographic phase as bulk materials. However, these methods suffer from the issues of precise control of thickness and reproducibility.

The solution-assisted and hydrothermal approaches are high-yield and low-cost methods for the synthesis and growth of BOXs nanosheets. Modification of the synthesis method can significantly alter the size and shape of the nanosheets. However, the solution-assisted synthesis approach suffers from the issue of intermediate phase formation during synthesis. CVD is the widely explored deposition technique used for the growth of BOXs with excellent control of surface morphology and thickness. It is a low-cost deposition method for large-scale high-quality thin films. MBE and PLD offer precise control over the epitaxial growth of high-quality, wafer-scale BOX thin films, paving the way for cost-effective industrial applications. Widespread adoption of these techniques is hindered by three key limitations: sophisticated instrumentation, high running costs, and the requirement for skilled professionals.

# 4. Sensing applications

Sensing can be applied for the detection of different analytes, molecules and radiation in different sensing media.[66–68] BOXs have gained huge attention for sensing applications due to their surface chemical reactivity and excellent charge transfer properties. These materials have been explored theoretically and experimentally for gas sensing, biosensing and optical sensing (photodetectors). Two-terminal chemiresistive, three-terminal FET and three-terminal electrochemical cell configurations are the popular device configurations for sensing applications. Based on sensing analytes using BOXs, these sensors can be broadly classified as gas sensors, biosensors and optical sensors. In the subsequent sections, we summarize most of the sensing applications reported for BOXs so far.

## 4.1 Gas sensing

Gas sensing is an important application to assure the quality of air in the surrounding atmosphere of the specimen. Gas sensors can detect specific gas molecules selectively for which they are designed. The gas-sensing phenomenon of semiconductor materials is governed either by physisorption or chemisorption activity over the material surface and the response is recorded in terms of change in the resistance of the device. Metal oxides have been the prime choice for sensing applications due to their excellent stability and sensitivity, but their high-temperature operation and poor selectivity are the limitations.[72,73] Over the last two decades, 2D materials have gained huge attention as a material of choice for gas sensing applications due to room temperature sensitivity and good selectivity.[74,75] Unlike other 2D materials, BOXs have not been explored to the best of their potential.

Xu *et al.* reported the detection of trace oxygen using 2D $Bi_2O_2Se$ nanoplates.[69] Representation of the device schematic and the dynamic sensing responses are given in Fig. 3a and b. The sensor shows an excellent limit of detection of 0.25 ppm for oxygen species and the detection range is from 0.25 to 400 ppm. The absorption of oxygen over the Se vacancies on the surface of $Bi_2O_2Se$ led to the change in resistance of the device. The sensing performance was tested for other gas molecules including $H_2$, Ar, $CO_2$, and $CH_4$ to confirm the selectivity of the device. The sensitivity of the device was very low for other gases compared with that for oxygen, where the concentration of each gas was kept at 3 ppm. The sensor shows good selectivity, sensitivity, and a wide detection range with excellent stability at room temperature. Furthermore, the improved sensing response was recorded by parallel integration of sensors to improve the signal-to-noise ratio for sub-ppm detection of oxygen.

Similarly, in 2023 Bae *et al.* reported the morphological dependence of the CVD-grown $Bi_2O_2Se$ nanostructures for oxygen sensing applications.[76] Among the three different morphologies (flakes, seed and bulk), vertical flakes show the highest sensing responses of 0.59% and 4.93% for 10 and 100 ppm, respectively, with excellent detection linearity for the 10 to 100 ppm range at an operating temperature of 100 °C. The vertical flake morphology also has the advantage of fast response and recovery over the other morphologies. The higher response of the flake morphology was due to the higher surface area of the topmost $Se^{2-}$ layer than that of other morphologies. The sensor shows good selectivity towards oxygen compared to 50 ppm of $CO_2$, $CH_2$, $H_2$, and $NO_2$, and humidity has a negligible effect on the sensing performance. The sensing reports on $Bi_2O_2Se$-based gas sensors show their potential to be used for the detection of trace oxygen in space and medical and semiconducting industries in the near future.

On the other hand, the first principles calculations reported for the $Bi_2O_2Se$ monolayer (ML) show the selective detection capabilities for NO and $NO_2$ detection due to lower absorption energy. Sirohi *et al.* calculated the interaction energies of the $Bi_2O_2Se$ ML and different gas molecules to determine the selectivity.[77] The vacancy less (VL) $Bi_2O_2Se$ ML layer shows selectivity towards $NO_2$ because of the lowest absorption energy of −0.48 eV. The $Bi_2O_2Se$ ML with Se vacancies (SV) shows the lowest absorption energy of −1.59 eV for NO gas molecules. Se vacancies enhance the selectivity and sensitivity of $Bi_2O_2Se$ MLs. Both VL and SV $Bi_2O_2Se$ MLs show good sensitivity towards NO gas molecules. Despite being relatively new and underexplored for gas sensing, BOXs materials like $Bi_2O_2Se$ MLs hold promise for detecting toxic gases according to theoretical calculations.

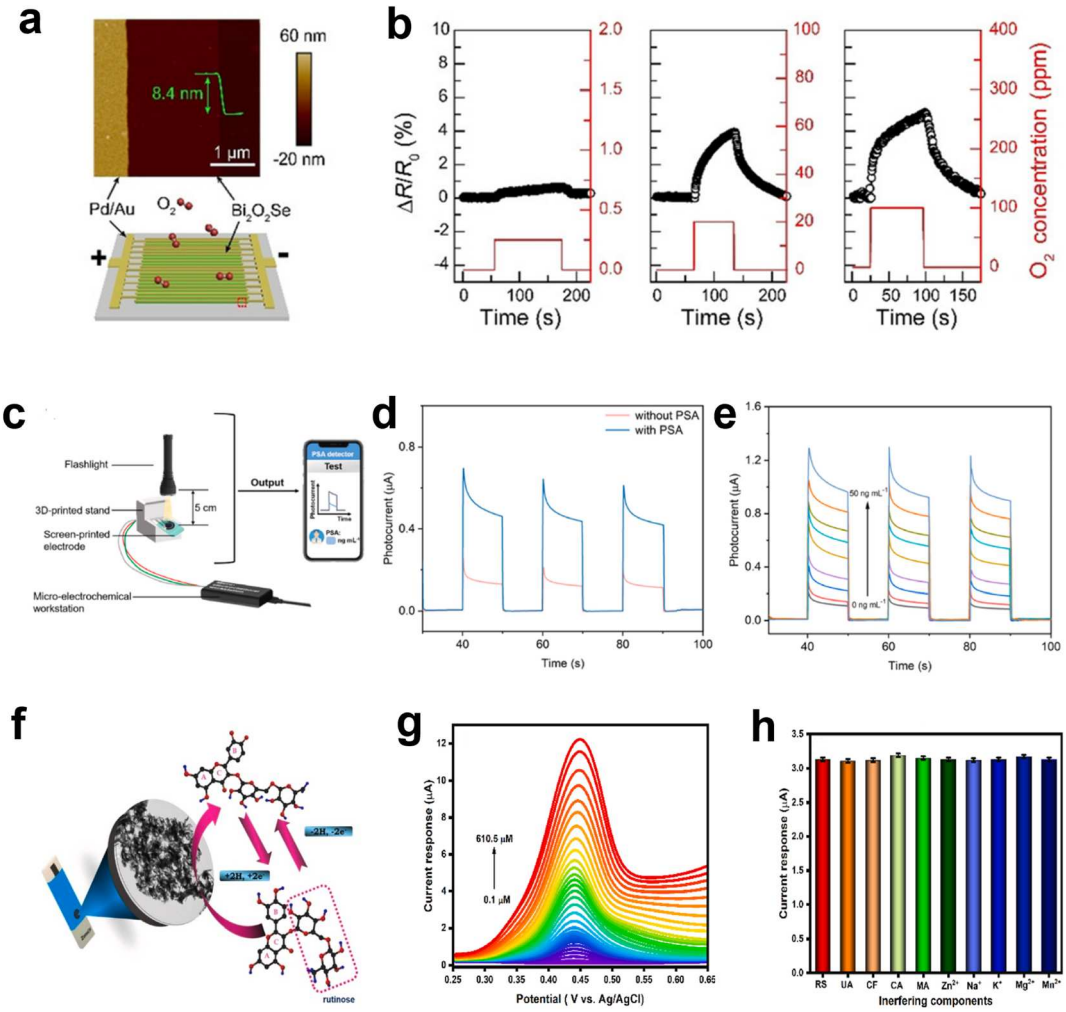


**Fig. 3** (a and b) The $Bi_2O_2Se$-based gas sensor for trace oxygen detection. Reproduced with permission.[69] Copyright 2022, Wiley-VCH. (c–e) The Co-doped $Bi_2O_2S$ biosensor for PSA detection. Reproduced with permission.[70] Copyright 2023, Elsevier. (f–h) Analgesic bioflavonoid detection using $Bi_2O_2S$. Reproduced with permission.[71] Copyright 2023, Elsevier.

Recently, Wei *et al.* explored the humidity detection performance of flexible resistive sensors using $Bi_2O_2S$ nanosheets.[78] The sensor shows excellent sensitivity of 2582 and fast response and recovery of 0.4 s and 2.4 s, respectively, for 84% RH. The sensor shows the potential for respiratory monitoring and noncontact human–machine interface applications.

### 4.2 Biosensing

Nanomaterials are being employed as electrode modifiers for the efficient detection of different biomarkers. In recent years, BOXs have drawn a lot of interest as electrode modifiers for the electrochemical detection of different biomarkers and analytes. Lin *et al.* reported the mobile-controlled portable detection of PSA using Co-doped $Bi_2O_2S$ nanosheets as a photoanode.[70] The sensing arrangement and responses are shown in Fig. 3c–e. The effect of Co-doping on the structural, morphological, optical and sensing properties was reported. The Co doping led to a reduced optical band gap from 0.90 eV to 0.86 eV upon 33% (CBOS-0.33) doping and increased photocurrent. The ascorbic acid generated through catalysis in the presence of PSA results in enhanced photocurrent. The CBOS-0.33 photoanode shows linear detection in the range of 0.2 to 50 ng $mL^{-1}$ and a LoD of 71.2 pg $ml^{-1}$.

Manickaraj *et al.* explored a modified approach (superficial-$CO_2$) for the synthesis of $Bi_2O_2S$ for the detection of rutinoside (RS).[71] The selective detection of analgesic bioflavonoids such as rutinoside (RS) is a great challenge. The conventional $Bi_2S_3$ (C-BiS) and superficial-$CO_2$ mediated $Bi_2O_2S$ (SC-BiOS) were studied as electrode modifiers. The observed results show the morphologies and crystallite sizes for both samples where C–BiS has a crystallite size of 11.57 nm with the formation of a nanorod-like morphology and SC-BiOS has a crystallite size of 9.03 nm with a nanopetal-like morphology. The SC-BiOS-modified electrode as shown in Fig. 3f has a higher surface area of 0.074 $cm^2$, lower transfer resistance and higher electron kinetics than the C-BiS-modified electrode. The SC-BiOS-modified electrode shows an excellent detection range of 0.1–610.5 μM

 

$L^{-1}$ (Fig. 3g) with detection limits of 9 and 30 nm $L^{-1}$ and a sensitivity of 0.706 μA μM $cm^{-2}$. The SC-BiOS shows good selectivity (Fig. 3h), repeatability, and recovery of 98.87% and can be used in real-time applications.

Similarly, Huang *et al.* studied Fe-loaded $Bi_2O_2S$ nanosheets for prostate-specific antigen (PSA) detection. PSA is secreted by cancer cells and in certain diseases, and PSA levels are high in the serum of patients having cancer.[79] Hence, the efficient detection of PSA levels can be useful in cancer diagnosis, treatment and monitoring. The developed sensing strategy involves the synthesis of Prussian blue (PB) nanoparticles by a liquid reaction method. Furthermore, the PS nanoparticles are bound by electrostatic absorption with signaling antibodies (mAb2). The trapped PSA by the trapping probe (mAb1) in a removable microplate forms a sandwich structure.

PB nanoparticles generate oxygen radicals due to the catalytic activity, and oxidation of 4-chloro-1-naphthol (4-CN) to benzo-4-chloro-hexadienone (4-CD) takes place. The transfer of 4-CD to the Fe-$Bi_2O_2S$ photoanode reduces the photocurrent as the concentration increases. The reported sensor shows a good dynamic detection range of 0.1 to 100 ng $ml^{-1}$ with a 34.2 pg $ml^{-1}$ limit of detection (LoD). The presented spilt incubation reaction strategy shows potential for large volume and low-cost detection of PSA. The sensor performance is comparable with that of the commercially available ELISA kits.

$Bi_2O_2Se$ nanoflowers with Au nanoparticles (AuNPs) have been reported for the detection of cancer cells (MCF-7).[81] Efficient determination of circulating tumor cells (CTC) will be a significant step towards reducing casualty due to cancer and increasing cancer survival rates. Photoelectrochemical sensing approaches have been widely studied for bioassay detection. An AuNPs/$Bi_2O_2S$/ITO photoanode was used as a sensing platform and the mercapto group aptamers (SH-Apt) were functionalized over the surface of the photoanode. The overexpressed protein in the cell membrane leads to the trapping of MCF-7 cells, and the level of MCF-7 cells significantly reduces the photocurrent. The sensor shows a linear detection range from 50 to $6 \times 10^5$ cells per mL with a detection limit of 17 cells per mL. The proposed sensing platform shows good sensitivity, selectivity and stability towards MCF-7 cell detection.

Wang *et al.* reported ultrasensitive biosensing properties of CVD-grown 2D $Bi_2O_2Te$ for the detection of biomolecules.[80] The alteration in the ferroelectric polarization of $Bi_2O_2Te$ upon interaction with miRNA led to a change in plasmonic response. The change in plasmonic response was recorded as a function of the concentration of miRNA487. The proposed sensor has an exceptionally lower LoD of 0.1 fM for miRNA487 and 1 fM for CEA biomolecules with good selectivity. The sensing performance of the $Bi_2O_2Te$ biosensor is shown in Fig. 4(a–c). Similarly, they explored the plasmonic detection properties of $Bi_2O_2Se$ for the detection of bovine serum albumin (BSA).[82] The sensor has a LoD of 1 fM for BSA with a short response time.

Shi *et al.* demonstrated a self-powered photoelectrochemical sensor for the selective and sensitive detection of tetracycline using a $Bi_2O_2S/Bi_2O_3$ heterostructure.[83] The sensor has a linear detection range from 0.1 pM to 200 nM and a LoD of 0.5 pM. $Bi_2O_2S$ nanosheets have been explored for the detection of cardiac troponin i and carcinoembryonic antigen with a good linear detection range.[84,85]

$H_2O_2$ is an important biomarker for the diagnosis of different diseases and the efficient detection of $H_2O_2$ has significant importance in healthcare, environmental and food industries. Chitara *et al.* reported the nonenzymatic electrochemical detection of $H_2O_2$ using 2D $Bi_2O_2Se$ nanosheets.[86] Cyclic voltammetry was employed to analyze the amount of $H_2O_2$ at a reduction potential of −0.68 V s Ag/AgCl in PBS buffer (pH 7.4). The $Bi_2O_2Se$ nanosheet modified GCE shows linear detection in the range of 50–500 μM with a sensitivity of 100 μA $mM^{-1}$ $cm^{-2}$. The selectivity of the sensor was analyzed with other interfering analytes like NaCl, dopamine, uric acid and ascorbic acid. The sensor shows excellent selectivity towards $H_2O_2$. Furthermore, the potential of this sensor for real-time application was studied using artificial sweat where the change in current was observed with the change in $H_2O_2$ concentration. The $H_2O_2$ detection capabilities of 2D $Bi_2O_2Se$ nanosheets show their potential to be used for the development of glucose sensors.

### 4.3 Optical sensing

Optical sensing or photodetection is an important category among all sensing applications. Optical sensors are devices used to detect a wide spectrum of electromagnetic radiation from ultraviolet (UV) to infrared (IR).[87,88] The development of optical sensors with broadband detection capabilities is a necessity of the modern era to facilitate advanced communication technologies. Over the years, a variety of semiconductor materials have been explored for photodetection, but 2D BOXs have gained huge attention in a few years for their application as a photodetector. The detection range of 2D TMDCs is limited up to the NIR region but the bandgap tunability of BOXs from 2.3 eV to 0.16 eV makes them suitable for broadband detection.[89,90]

2D $Bi_2O_2Se$ is the most popular and extensively studied material for optoelectronic applications in the BOX family.[91] Wu *et al.* reported the first photodetection using $Bi_2O_2Se$. The device shows excellent responsivity of 2000 A $W^{-1}$ at 532 nm wavelength.[92] Khan *et al.* reported that the gate tunable $Bi_2O_2Se$ phototransistor has a maximum responsivity of 22 100 A $W^{-1}$ and photoconductivity of $3.4 \times 10^{15}$ Jones with an on/off ratio of $10^9$.[56] The tuning of photocurrent using gate voltage significantly reduced the high dark current and hence a high on/off ratio was achieved. The band gap of $Bi_2O_2Se$ is suitable for detection in the IR region, which the conventional silicon-based devices are unable to detect. Yin *et al.* tried for the first time to extend the detection wavelength up to 1700 nm using 2D $Bi_2O_2Se$.[93] They observed responsivity values of 5800 A $W^{-1}$, 4 A $W^{-1}$ and 0.1 A $W^{-1}$ for 532 nm, 1310 nm and 1550 nm wavelengths, respectively. Furthermore, Chen *et al.* reported the IR to THz detection, where the proposed mechanism shows that the generation of carriers is due to absorption for the IR region and electromagnetically induced well-injected

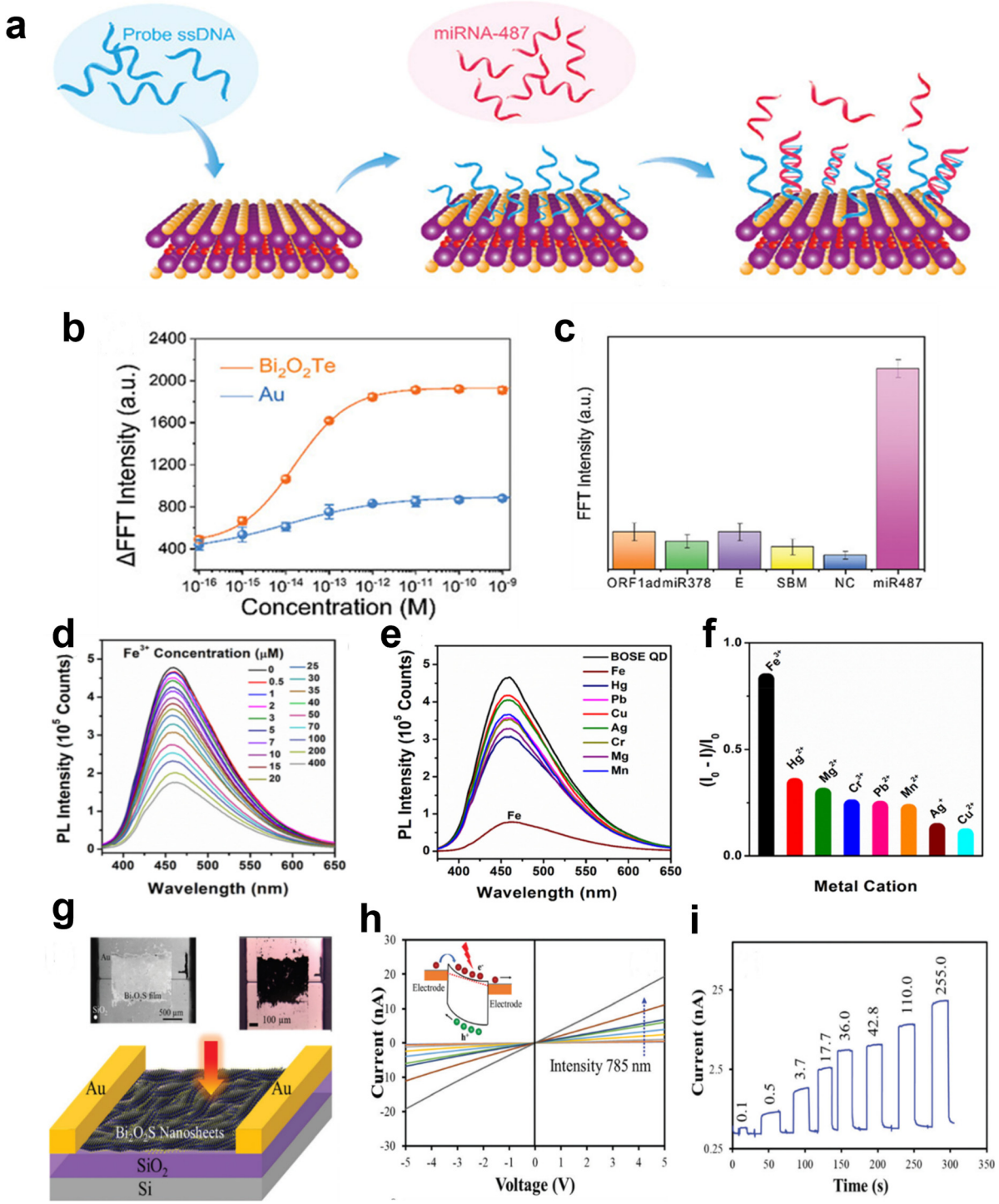


**Fig. 4** (a–c) The $Bi_2O_2Te$-based plasmonic sensor for detection of miRNA487. Reproduced with permission.[80] Copyright 2024, Wiley-VCH. (d–f) $Bi_2O_2Se$ QDs for detection of heavy metal ions. Reproduced with permission.[61] Copyright 2023, Royal Society of Chemistry. (g–i) NIR photodetection using $Bi_2O_2S$ nanosheets. Reproduced with permission.[67] Copyright 2023, Royal Society of Chemistry.

electrons for the THz region.[55] The responsivity of the device was reported as 50 A $W^{-1}$ at 1550 nm and $10^4$ V $W^{-1}$ at 0.17 THz.

Tian *et al.* reported the photodetection performance of 2D $Bi_2O_2Te$ grown on a Si substrate. The sputtered $Bi_2Te_3$ layer was annealed for 10 min at 400 °C under atmospheric conditions for transformation to $Bi_2O_2Te$.[59] The device shows good detection in the range from UV (210 nm) to SWIR (2400 nm). A responsivity of $3 \times 10^5$ A $W^{-1}$ was reported for UV while $2 \times 10^4$ A $W^{-1}$ for SWIR. Later, Yang *et al.* reported a self-

powered photoelectrochemical photodetector based on 2D $Bi_2O_2Te$ cells with a quasi-solid electrolyte. The reported device shows a responsivity of 20.5 mA $W^{-1}$ (zero bias) and fast rise/decay times of 6/90 ms under 365 nm irradiation.[94] Apart from pristine BOXs, various 2D/2D heterostructured configurations have also been studied for improved device performance and low dark current.[94]

Paul *et al.* explored the detection of heavy metal ions using $Bi_2O_2Se$ quantum dots (QDs) as shown in Fig. 4(d–f). $Bi_2O_2Se$ QDs of nanometric dimensions were prepared *via* a top-down chemical approach.[61] The $Bi_2O_2Se$ QDs show selective detection of $Fe^{3+}$ ions as a function of fluorescence quenching. The DFT calculations show that the quenching takes place due to the interaction between Fe and Se ions.

Fig. 4(g–i) present the device schematic and photodetection performance of the 2D $Bi_2O_2S$ nanosheet-based broadband photodetector.[67] Hydrothermally grown 2D $Bi_2O_2S$ flowers on a FTO substrate have been reported for the detection of NIR wavelength (850 nm) with an excellent responsivity of 9.48 mA $W^{-1}$, a specific detectivity of 9.96 × $10^{10}$ Jones and a fast response time of 227.7 ms.[50] The fabricated device shows good environmental stability.

## 5. Strategies for improved device performance

The sensing performance of 2D BOXs can be improved through the following strategies:

### 5.1 Controlled growth

The controlled growth of semiconductor materials is an important parameter for sensing applications. The sensing performance of a material depends on the active sites and hence

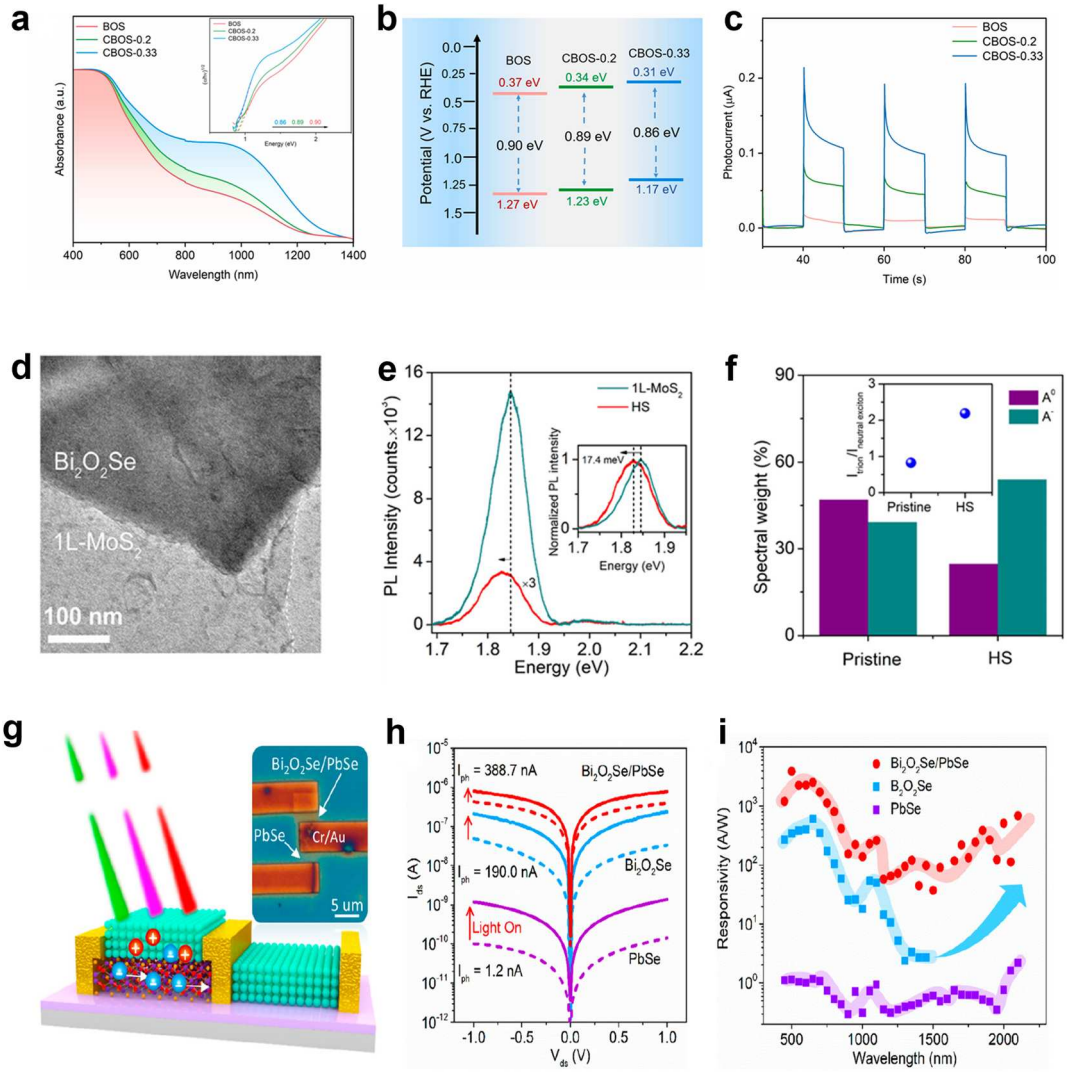


**Fig. 5** (a–c) Tuning of optical and electronic properties of Co-doped $Bi_2O_2S$ nanosheets. Reproduced with permission.[70] Copyright 2023, Elsevier. (d–f) 2D/2D $MoS_2/Bi_2O_2Se$ heterojunction.[95] Copyright 2023, American Chemical Society. (g–i) The PbSe QD modified $Bi_2O_2Se$ photodetector. Reproduced with permission.[96] Copyright 2019, American Chemical Society.

defect density. The defect-induced modulation of electronic properties causes significant alteration in sensing properties. In the discussion of sensing applications, the Se vacancies significantly alter the sensing performance of the device. Furthermore, surface morphologies also correlate with the sensing performance and hence controlled growth is a must for reproducible devices with similar performance.

### 5.2 Doping

Doping is a well-established approach for tuning the semiconducting properties of materials. Substitutional doping significantly alters the surface absorption energies and can help to improve the sensing performance. So far, doping in BOXs has not been explored properly. The doping strategies and their effect on fundamental properties reported recently for sensing applications show significant improvement as shown in Fig. 5 (a–c).[37] There are other reports available on doping for catalytic and energy applications.[97,98]

### 5.3 Heterostructures or composites

The combination of BOXs with other suitable materials can be a suitable strategy to improve device performance. It involves heterojunction formation, surface functionalization, decoration and mixing with other materials of different or the same dimensionality. The heterojunction formation between other 2D materials and BOXs shows improved charge transfer as shown in Fig. 5(d–f).[95] It can further resolve the issue of large dark current in photodetection devices. CVD is one of the promising techniques for the controlled growth of BOX heterojunctions. Wet and dry transfer, drop casting, and hydrothermal and mechanical mixing also have the potential to be used to form heterostructures and composites. Decoration with lower dimensional materials can also be a significant approach to improve the sensing performance (Fig. 5(g–i)).[96]

For real-time sensing applications, a sensor needs to meet the various figures of merit including sensitivity, selectivity and operating temperature. These parameters depend on the properties of the sensing layer. The formation of heterostructures can improve the sensing performance because they have a significant effect on the various functions involved in the sensing process. 2D BOX nanosheets have a large surface-to-volume ratio and active sites for absorption. The formation of heterostructures with other materials can tune the interaction ability and selectivity of the specific gas. The change in carrier concentration and the built-in potential at the interface of a heterostructure significantly alters the sensing ability and signal conversion performance of the sensor. Hence, the design of 2D BOX heterostructures with receptor materials can significantly improve the sensing response. Table 1 summarises the recent studies published on BOXs-based sensing applications.

## 6. Conclusion and outlook

This mini-review highlights the promising applications of BOX materials in next-generation flexible and wearable electronics, particularly for sensing. To address this potential, we discussed various recent advancements in synthesis and growth techniques. We also explored the structural, electronic, and charge properties of BOXs, along with their dependence on thickness. BOXs have ultrahigh carrier mobility, excellent stability and band gap tunability up to 0.16 eV compared to conventional 2D materials. Due to these excellent material properties, 2D BOXs have been studied for different electronic applications, including sensing, photodetection, transistors and logic devices. In the BOX family, the 2D $Bi_2O_2Se$ nanosheet material is the most reported and studied member. It has been extensively studied for photodetection applications. As known, this is a relatively new category of semiconductor materials and hence it is less explored for gas sensing and biosensing applications. In this review, we dis-

**Table 1** Comparison of the sensing studies using BOXs

| Sensing category | Material | Sensing mechanism | Detection species | Ref. |
|---|---|---|---|---|
| Gas sensing | $Bi_2O_2Se$ | Resistive sensing | $O_2$ | 69 |
| | $Bi_2O_2Se$ | Resistive sensing | $O_2$ | 76 |
| | $Bi_2O_2Se$ (theoretical) | Resistive sensing | $NO_2$ and NO | 77 |
| | $Bi_2O_2S$ | Resistive sensing | Humidity | 78 |
| Biosensing | $Bi_2O_2Te$ | Plasmonic detection | miRNA487 | 80 |
| | $Bi_2O_2Se$ | Plasmonic detection | BSA | 82 |
| | $Bi_2O_2S$ | Photoelectrochemical | MCF-7 | 81 |
| | Fe-$Bi_2O_2S$ | Photoelectrochemical | PSA | 79 |
| | $Ag_2O$-$Bi_2O_2S$ | Photoelectrochemical | PSA | 99 |
| | Co-$Bi_2O_2S$ | Photoelectrochemical | PSA | 70 |
| | $Bi_2O_2S$/$Bi_2O_3$ | Photoelectrochemical | Tetracycline | 83 |
| | $Bi_2O_2S$ | Electrochemical | Bioflavonoid | 71 |
| | $Bi_2O_2Se$ | Electrochemical | $H_2O_2$ | 86 |
| Optical sensing | $Bi_2O_2S$ | Photodetector | NIR | 67 |
| | $Bi_2O_2Se$ | Photodetector | SWIR | 100 |
| | $Bi_2O_2Te$ | Photodetector | SWIR | 101 |
| | $Bi_2O_2Se$ | Fluorescence | $Fe^{3+}$ | 61 |

cussed the reported experimental and theoretical studies on sensing applications. Based on observation during the preparation of this article, the following avenues can be explored for the development of efficient sensing devices: (1) theoretically BOXs-based gas sensors have low absorption energies for $NO_2$ and NO gas molecules and hence these can be explored for sensing device optimization. (2) The experimental reports show that the significant surface and band gap tunability of these materials can provide a useful strategy for the development of efficient sensing devices for environmental and health monitoring.

BOX nanosheets can be a material of choice because of their excellent electronic properties for gas sensing, biosensing and optical detection. These materials are promising candidates for downscaled sensors due to their potential for tailoring properties through doping, defect introduction, and functionalization, leading to enhanced selectivity and sensitivity. The controlled alteration or modification can improve the surface reactivity for the target species for detection. 2D BOXs hold significant promise for multifunctional applications in commercial electronics, but their full potential remains untapped. Collaborative efforts between academic and industry can accelerate development and overcome current limitations, paving the way for future breakthroughs.

## Conflicts of interest

There are no conflicts to declare.

## Acknowledgements

The authors are thankful for the financial support by the U.S. National Science Foundation (Award #2122044). This research was partially sponsored by the Army Research Office (ARO) and was accomplished under Grant W911NF2210109. The views and conclusions contained in this document are those of the authors and should not be interpreted as representing the official policies, either expressed or implied, of the ARO or the U.S. Government. The U.S. Government is authorized to reproduce and distribute reprints for Government purposes notwithstanding any copyright notation herein.

## References

1 J. S. Kilby, *IEEE Trans. Electron Devices*, 1976, **23**, 648–654.
2 International Roadmap for Devices and Systems (IRDSTM) 2020 Edition – IEEE IRDSTM, **https://irds.ieee.org/editions/2020**.
3 A. D. Franklin, *Science*, 2015, **349**, 6249.
4 M. Long, P. Wang, H. Fang and W. Hu, *Adv. Funct. Mater.*, 2019, **29**, 1803807.
5 C. Wu, X. Zhang, R. Wang, L. J. Chen, M. Nie, Z. Zhang, X. Huang and L. Han, *Nanotechnology*, 2021, **33**, 072001.
6 M. R. Kumar, S. Singh, H. M. Fahmy, N. K. Jaiswal, S. Akin, A. E. Shalan, S. Lanceros-Mendez and M. Salado, *J. Power Sources*, 2023, **556**, 232256.
7 C. C. Chiang, V. Ostwal, P. Wu, C. S. Pang, F. Zhang, Z. Chen and J. Appenzeller, *Appl. Phys. Rev.*, 2021, **8**, 021306.
8 K. S. Novoselov, A. K. Geim, S. V. Morozov, D. Jiang, Y. Zhang, S. V. Dubonos, I. V. Grigorieva and A. A. Firsov, *Science*, 2004, **306**, 666–669.
9 L. Li, W. Han, L. Pi, P. Niu, J. Han, C. Wang, B. Su, H. Li, J. Xiong, Y. Bando and T. Zhai, *InfoMat*, 2019, **1**, 54–73.
10 C. Liu, H. Chen, S. Wang, Q. Liu, Y. G. Jiang, D. W. Zhang, M. Liu and P. Zhou, *Nat. Nanotechnol.*, 2020, **15**, 545–557.
11 L. Pi, L. Li, K. Liu, Q. Zhang, H. Li and T. Zhai, *Adv. Funct. Mater.*, 2019, **29**, 1904932.
12 Y. Pei, X. Zhang, Z. Hui, J. Zhou, X. Huang, G. Sun and W. Huang, *ACS Nano*, 2021, **15**, 3996–4017.
13 Y. Li, M. Gu, X. Zhang, J. Fan, K. Lv, S. A. C. Carabineiro and F. Dong, *Mater. Today*, 2020, **41**, 270–303.
14 M. Luo, T. Fan, Y. Zhou, H. Zhang and L. Mei, *Adv. Funct. Mater.*, 2019, **29**, 1808306.
15 K. Zhang, Y. Feng, F. Wang, Z. Yang and J. Wang, *J. Mater. Chem. C*, 2017, **5**, 11992–12022.
16 R. Samal, G. Sanyal, B. Chakraborty and C. S. Rout, *J. Mater. Chem. A*, 2021, **9**, 2560–2591.
17 R. Prasanna, A. Gold-Parker, T. Leijtens, B. Conings, A. Babayigit, H. G. Boyen, M. F. Toney and M. D. McGehee, *J. Am. Chem. Soc.*, 2017, **139**, 11117–11124.
18 X. Duan, C. Wang, A. Pan, R. Yu and X. Duan, *Chem. Soc. Rev.*, 2015, **44**, 8859–8876.
19 X. Cui, G. H. Lee, Y. D. Kim, G. Arefe, P. Y. Huang, C. H. Lee, D. A. Chenet, X. Zhang, L. Wang, F. Ye, F. Pizzocchero, B. S. Jessen, K. Watanabe, T. Taniguchi, D. A. Muller, T. Low, P. Kim and J. Hone, *Nat. Nanotechnol.*, 2015, **10**, 534–540.
20 D. Jariwala, V. K. Sangwan, L. J. Lauhon, T. J. Marks and M. C. Hersam, *ACS Nano*, 2014, **8**, 1102–1120.
21 T. Ohta, A. Bostwick, T. Seyller, K. Horn and E. Rotenberg, *Science*, 2006, **313**, 951–954.
22 F. Schwierz, *Nat. Nanotechnol.*, 2010, **5**, 487–496.
23 S. Zhang, J. Yang, R. Xu, F. Wang, W. Li, M. Ghufran, Y. W. Zhang, Z. Yu, G. Zhang, Q. Qin and Y. Lu, *ACS Nano*, 2014, **8**, 9590–9596.
24 F. Xia, H. Wang and Y. Jia, *Nat. Commun.*, 2014, **5**, 1–6.
25 F. Wang, S. Yang, J. Wu, X. Hu, Y. Li, H. Li, X. Liu, J. Luo and T. Zhai, *InfoMat*, 2021, **3**, 1251–1271.
26 M. T. Hossain, T. Jena and P. K. Giri, *Small Struct.*, 2024, 2300511.
27 D. Verma, B. Liu, T. C. Chen, L. J. Li and C. S. Lai, *Nanoscale Adv.*, 2022, **4**, 3832–3844.
28 J. Wu, H. Yuan, M. Meng, C. Chen, Y. Sun, Z. Chen, W. Dang, C. Tan, Y. Liu, J. Yin, Y. Zhou, S. Huang, H. Q. Xu, Y. Cui, H. Y. Hwang, Z. Liu, Y. Chen, B. Yan and H. Peng, *Nat. Nanotechnol.*, 2017, **12**, 530–534.

29 Y. Liang, Y. Chen, Y. Sun, S. Xu, J. Wu, C. Tan, X. Xu, H. Yuan, L. Yang, Y. Chen, P. Gao, J. Guo and H. Peng, *Adv. Mater.*, 2019, **31**, 1901964.
30 C. Tan, M. Tang, J. Wu, Y. Liu, T. Li, Y. Liang, B. Deng, Z. Tan, T. Tu, Y. Zhang, C. Liu, J. H. Chen, Y. Wang and H. Peng, *Nano Lett.*, 2019, **19**, 2148–2153.
31 Q. Wei, R. Li, C. Lin, A. Han, A. Nie, Y. Li, L. J. Li, Y. Cheng and W. Huang, *ACS Nano*, 2019, **13**, 13439–13444.
32 M. Wu and X. C. Zeng, *Nano Lett.*, 2017, **17**, 6309–6314.
33 X. Yang, L. Qu, F. Gao, Y. Hu, H. Yu, Y. Wang, M. Cui, Y. Zhang, Z. Fu, Y. Huang, W. Feng, B. Li and P. Hu, *ACS Appl. Mater. Interfaces*, 2022, **14**, 7175–7183.
34 X. Zhang, Y. Liu, G. Zhang, Y. Wang, H. Zhang and F. Huang, *ACS Appl. Mater. Interfaces*, 2015, **7**, 4442–4448.
35 M. T. Hossain, T. Jena, U. Nath, M. Sarma and P. K. Giri, *Nanoscale*, 2023, **15**, 11222–11236.
36 M. T. Hossain, T. Jena, S. Debnath and P. K. Giri, *J. Mater. Chem. C*, 2023, **11**, 6670–6684.
37 M. Q. Li, L. Y. Dang, G. G. Wang, F. Li, M. Han, Z. P. Wu, G. Z. Li, Z. Liu and J. C. Han, *Adv. Mater. Technol.*, 2020, **5**, 2000180.
38 W. Ai, J. Chen, X. Dong, Z. Gao, Y. He, Z. Liu, H. Fu, F. Luo and J. Wu, *Nano Lett.*, 2022, **22**, 7659–7666.
39 L. Xu, S. Liu, H. Zhang, X. Zhang, J. Li, J. Yan, B. Shi, J. Yang, C. Yang, L. Xu, X. Sun and J. Lu, *Phys. Chem. Chem. Phys.*, 2020, **22**, 7853–7863.
40 J. Wu, C. Tan, Z. Tan, Y. Liu, J. Yin, W. Dang, M. Wang and H. Peng, *Nano Lett.*, 2017, **17**, 3021–3026.
41 H. Fu, J. Wu, H. Peng and B. Yan, *Phys. Rev. B*, 2018, **97**, 241203(R), DOI: **10.1103/PhysRevB.97.241203**.
42 T. Tong, M. Zhang, Y. Chen, Y. Li, L. Chen, J. Zhang, F. Song, X. Wang, W. Zou, Y. Xu and R. Zhang, *Appl. Phys. Lett.*, 2018, **113**, 072106, DOI: **10.1063/1.5042727**.
43 X. Zou, F. Tian, H. Liang, Y. Li, Y. Sun and C. Wang, *ACS Nano*, 2022, **16**, 19543–19550.
44 T. Ghosh, M. Samanta, A. Vasdev, K. Dolui, J. Ghatak, T. Das, G. Sheet and K. Biswas, *Nano Lett.*, 2019, **19**, 5703–5709.
45 C. Chen, M. Wang, J. Wu, H. Fu, H. Yang, Z. Tian, T. Tu, H. Peng, Y. Sun, X. Xu, J. Jiang, N. B. M. Schröter, Y. Li, D. Pei, S. Liu, S. A. Ekahana, H. Yuan, J. Xue, G. Li, J. Jia, Z. Liu, B. Yan, H. Peng and Y. Chen, *Sci. Adv.*, 2018, **4**, eaat8355.
46 P. Li, A. Han, C. Zhang, X. He, J. Zhang, D. Zheng, L. Cheng, L. J. Li, G. X. Miao and X. X. Zhang, *ACS Nano*, 2020, **14**, 11319–11326.
47 X. Mu, C. Li, L. Wang, R. Zhang, Y. Huang, X. Yu, P. K. Wong and L. Ye, *J. Hazard. Mater.*, 2022, **440**, 129808.
48 H. Xie, M. Liu, B. You, G. Luo, Y. Chen, B. Liu, Z. Jiang, P. K. Chu, J. Shao and X. F. Yu, *Small*, 2020, **16**, 1905208.
49 K. Zhang, C. Hu, X. Kang, S. Wang, Y. Xi and H. Liu, *Mater. Res. Bull.*, 2013, **48**, 3968–3972.
50 P. Rong, S. Gao, M. Zhang, S. Ren, H. Lu, J. Jia, S. Jiao, Y. Zhang and J. Wang, *J. Alloys Compd.*, 2022, **928**, 167128.
51 W. Zhang, D. Liu, W. Jin, D. Zhang, T. Sun, E. Liu, X. Hu and H. Miao, *Int. J. Hydrogen Energy*, 2024, **51**, 1545–1557.
52 G. Zhang, N. Zhao, K. Wang and J. Li, *Appl. Phys. A: Mater. Sci. Process.*, 2023, **129**, 1–9.
53 B. Chitara, A. K. Shringi, B. Roy, M. H. Wu and F. Yan, *Mater. Lett.*, 2023, **346**, 134545.
54 P. C. Kumar, S. Senapati, D. Pradhan, J. Kumar and R. Naik, *J. Alloys Compd.*, 2023, **968**, 172166.
55 Y. Chen, W. Ma, C. Tan, M. Luo, W. Zhou, N. Yao, H. Wang, L. Zhang, T. Xu, T. Tong, Y. Zhou, Y. Xu, C. Yu, C. Shan, H. Peng, F. Yue, P. Wang, Z. Huang and W. Hu, *Adv. Funct. Mater.*, 2021, **31**, 2009554.
56 U. Khan, Y. Luo, L. Tang, C. Teng, J. Liu, B. Liu and H. M. Cheng, *Adv. Funct. Mater.*, 2019, **29**, 1807979.
57 J. C. Park, S. Kim, H. Choi, Y. Jung, I. Oh, J. B. Hwang and S. Lee, *Cryst. Growth Des.*, 2023, **23**, 2092–2098.
58 Y. Song, Z. Li, H. Li, S. Tang, G. Mu, L. Xu, W. Peng, D. Shen, Y. Chen, X. Xie and M. Jiang, *Nanotechnology*, 2020, **31**, 165704.
59 P. Tian, H. Wu, L. Tang, J. Xiang, R. Ji, S. P. Lau, K. S. Teng, W. Guo, Y. Yao and L. J. Li, *J. Mater. Chem. C*, 2021, **9**, 13713–13721.
60 M. Kang, H. J. Chai, H. B. Jeong, C. Park, I. Y. Jung, E. Park, M. M. Çiçek, I. Lee, B. S. Bae, E. Durgun, J. Y. Kwak, S. Song, S. Y. Choi, H. Y. Jeong and K. Kang, *ACS Nano*, 2021, **15**, 8715–8723.
61 S. Paul, S. Nandi, M. Das, A. Bora, M. T. Hossain, S. Ghosh and P. K. Giri, *Nanoscale*, 2023, **15**, 12612–12625.
62 L. Pan, L. Zhao, X. Zhang, C. Chen, P. Yao, C. Jiang, X. Shen, Y. Lyu, C. Lu, L. D. Zhao and Y. Wang, *ACS Appl. Mater. Interfaces*, 2019, **11**, 21603–21609.
63 Z. Hui, X. Bu, Y. Wang, D. Han, J. Gong, L. Li, X. Li and S. Yan, *Adv. Opt. Mater.*, 2022, **10**, 2201812.
64 A. Bora, S. Paul, M. T. Hossain and P. K. Giri, *J. Phys. Chem. C*, 2022, **126**, 12623–12634.
65 C. Huang and H. Yu, *ACS Appl. Mater. Interfaces*, 2020, **12**, 19643–19654.
66 A. K. Shringi, R. Kumar, N. F. Dennis and F. Yan, *Chemosensors*, 2024, **12**, 17.
67 B. Chitara, T. B. Limbu, J. D. Orlando, Y. Tang and F. Yan, *Nanoscale*, 2020, **12**, 16285–16291.
68 M. Das, A. K. Shringi and M. Kumar, *IEEE Sens. J.*, 2022, **22**, 19183–19190.
69 S. Xu, H. Fu, Y. Tian, T. Deng, J. Cai, J. Wu, T. Tu, T. Li, C. Tan, Y. Liang, C. Zhang, Z. Liu, Z. Liu, Y. Chen, Y. Jiang, B. Yan and H. Peng, *Angew. Chem., Int. Ed.*, 2020, **59**, 17938–17943.
70 Q. Lin, Z. Yu, L. Lu, X. Huang, Q. Wei and D. Tang, *Biosens. Bioelectron.*, 2023, **230**, 115260.
71 S. S. M. Manickaraj, S. Pandiyarajan, A. H. Liao, A. R. Panneer Selvam, S. T. Huang, J. R. Vimala, K. Y. Lee and H. C. Chuang, *Chemosphere*, 2023, **328**, 138534.
72 V. S. Bhati, M. Kumar and R. Banerjee, *J. Mater. Chem. C*, 2021, **9**, 8776–8808.
73 A. Dey, *Mater. Sci. Eng., B*, 2018, **229**, 206–217.
74 A. Kumar, A. Mirzaei, M. H. Lee, Z. Ghahremani, T. U. Kim, J. Y. Kim, M. Kwoka, M. Kumar, S. S. Kim and H. W. Kim, *J. Mater. Chem. A*, 2024, **12**, 3771–3806.


 

75 X. Liu, T. Ma, N. Pinna and J. Zhang, *Adv. Funct. Mater.*, 2017, **27**, 1702168.
76 J. K. Bae, H. H. Cho, H. Shin, Y. Kim, H. Ko, S. J. Lee, D. D. Megersa, G. T. Gudena, S. Chae, I. S. Cho and H. K. Yu, *Sens. Actuators, B*, 2023, **394**, 134398.
77 A. Sirohi and J. Singh, *IEEE Trans. Nanotechnol.*, 2022, **21**, 794–800.
78 C. Wei, M. Zhu, Z. Zhou, S. Zhao, J. Mao, D. Yin, J. Li, Y. Wang and J. Hao, *Chem. Eng. J.*, 2021, **420**, 127655.
79 X. Huang, Q. Lin, H. Gong, L. Lu, Q. Wei and D. Tang, *Anal. Chim. Acta*, 2023, **1252**, 341058.
80 Z. Wang, L. Liu, P. Li, A. Nie, K. Zhai, J. Xiang, C. Mu, F. Wen, B. Wang, T. Xue and Z. Liu, *Small*, 2024, 2312175.
81 X. Xu, Z. Ding, X. Zhang, R. Zha, W. Li, L. Xu, D. Sun, X. Cai, T. Liang, Y. Wang and C. Li, *Anal. Chim. Acta*, 2023, **1251**, 340982.
82 Z. Wang, L. Liu, K. Zhai, A. Nie, J. Xiang, C. Mu, F. Wen, B. Wang, Y. Shu, T. Xue and Z. Liu, *Small*, 2023, **19**, 2303026.
83 B. Shi, B. Chen, X. Yan, H. Cao, H. Sun, D. Wang, C. Bi, C. Wang, Y. Wang, C. Dai and W. Liu, *Mater. Des.*, 2024, **239**, 112781.
84 Z. Yu, Q. Lin, H. Gong, M. Li and D. Tang, *Biosens. Bioelectron.*, 2023, **223**, 115028.
85 L. Chi, X. Wang, H. Chen, D. Tang and F. Xue, *J. Mater. Chem. B*, 2022, **10**, 10018–10026.
86 B. Chitara, T. B. Limbu, J. D. Orlando, K. Vinodgopal and F. Yan, *IEEE Sens. Lett.*, 2020, **4**, 2000504.
87 J. Yao and G. Yang, *Nanoscale*, 2020, **12**, 454–476.
88 X. Guan, X. Yu, D. Periyanagounder, M. R. Benzigar, J. K. Huang, C. H. Lin, J. Kim, S. Singh, L. Hu, G. Liu, D. Li, J. H. He, F. Yan, Q. J. Wang and T. Wu, *Adv. Opt. Mater.*, 2021, **9**, 2001708.
89 A. Parida, S. Senapati and R. Naik, *Mater. Today Chem.*, 2022, **26**, 101149.
90 F. Wang, S. Yang, J. Wu, X. Hu, Y. Li, H. Li, X. Liu, J. Luo and T. Zhai, *InfoMat*, 2021, **3**, 1251–1271.
91 T. Li and H. Peng, *Acc. Mater. Res.*, 2021, **2**, 842–853.
92 W. Wu, J. Yu, Y. H. Chen, Y. Liu, S. Cheng, Y. Lai, J. Sun, H. Zhou and K. He, *ACS Nano*, 2023, **17**, 16633–16643.
93 J. Yin, Z. Tan, H. Hong, J. Wu, H. Yuan, Y. Liu, C. Chen, C. Tan, F. Yao, T. Li, Y. Chen, Z. Liu, K. Liu and H. Peng, *Nat. Commun.*, 2018, **9**, 1–7.
94 S. Yang, S. Jiao, Y. Nie, Y. Zhao, S. Gao, D. Wang and J. Wang, *Mater. Horiz.*, 2024, **11**, 1710–1718.
95 M. T. Hossain, L. P. L. Mawlong, T. Jena, A. Bora, U. Nath, M. Sarma and P. K. Giri, *ACS Appl. Nano Mater.*, 2023, **6**, 11023–11036.
96 P. Luo, F. Zhuge, F. Wang, L. Lian, K. Liu, J. Zhang and T. Zhai, *ACS Nano*, 2019, **13**, 9028–9037.
97 Y. Luo, H. Han, J. Li, Q. Wang, W. Zhang and Y. Jia, *Sep. Purif. Technol.*, 2023, **306**, 122734.
98 Y. Xing, X. Jiang, L. Han, X. Jin, G. Ni, Y. Peng, X. Yong and X. Wang, *J. Cleaner Prod.*, 2023, **400**, 136631.
99 X. Huang, L. Lu, Q. Lin, Q. Wei and D. Tang, *Biosens. Bioelectron.*, 2023, **239**, 115608.
100 J. Yin, Z. Tan, H. Hong, J. Wu, H. Yuan, Y. Liu, C. Chen, C. Tan, F. Yao, T. Li, Y. Chen, Z. Liu, K. Liu and H. Peng, *Nat. Commun.*, 2018, **9**, 1–7.
101 P. Tian, H. Wu, L. Tang, J. Xiang, R. Ji, S. P. Lau, K. S. Teng, W. Guo, Y. Yao and L. J. Li, *J. Mater. Chem. C*, 2021, **9**, 13713–13721.